Optics Letters

Micro-pulse upconversion Doppler lidar for wind and visibility detection in the atmospheric boundary layer

Haiyun Xia,[1,2,3] Mingjia Shangguan,[3,4] Chong Wang,[1] Guoliang Shentu,[3,4] Jiawei Qiu,[1] Qiang Zhang,[3,4,5] Xiankang Dou,[1,*] and Jianwei Pan[3,4]

[1]CAS Key Laboratory of Geospace Environment, University of Science and Technology of China, Hefei 230026, China
[2]Collaborative Innovation Center of Astronautical Science and Technology, Harbin Institute of Technology, Harbin 150001, China
[3]Synergetic Innovation Center of Quantum Information and Quantum Physics, USTC, Hefei 230026, China
[4]Shanghai Branch, National Laboratory for Physical Sciences at Microscale and Department of Modern Physics, USTC, Shanghai 201315, China
[5]Jinan Institute of Quantum Technology, Jinan, Shandong 250101, China
*Corresponding author: dou@ustc.edu.cn

Received 24 August 2016; revised 8 October 2016; accepted 10 October 2016; posted 13 October 2016 (Doc. ID 274371); published 7 November 2016

For the first time, to the best of our knowledge, a compact, eye-safe, and versatile direct detection Doppler lidar is developed using an upconversion single-photon detection method at 1.5 μm. An all-fiber and polarization maintaining architecture is realized to guarantee the high optical coupling efficiency and the robust stability. Using integrated-optic components, the conservation of etendue of the optical receiver is achieved by manufacturing a fiber-coupled periodically poled lithium niobate waveguide and an all-fiber Fabry–Perot interferometer (FPI). The double-edge technique is implemented by using a convert single-channel FPI and a single upconversion detector, incorporating a time-division multiplexing method. The backscatter photons at 1548.1 nm are converted into 863 nm via mixing with a pump laser at 1950 nm. The relative error of the system is less than 0.1% over nine weeks. In experiments, atmospheric wind and visibility over 48 h are detected in the boundary layer. The lidar shows good agreement with the ultrasonic wind sensor, with a standard deviation of 1.04 m/s in speed and 12.3° in direction.

OCIS codes: (010.3640) Lidar; (010.0280) Remote sensing and sensors; (190.7220) Upconversion; (280.3340) Laser Doppler velocimetry.

http://dx.doi.org/10.1364/OL.41.005218

As the atmospheric boundary layer (ABL) affects both the dynamics and thermodynamics of the atmosphere, it plays an important role in many fields, such as air pollution and the dispersal of pollutants, agricultural meteorology, hydrology, numerical weather prediction, climate simulation, and aeronautical meteorology. For example, in air quality control and management, to understand the transport and dispersal processes that affect the concentrations of atmospheric pollutants, one needs knowledge of dynamic and mixing conditions, including the wind speed and direction profiles, the strength of turbulence, and the structure of the ABL [1]. In aeronautical applications, the detections of boundary-layer phenomena, such as low cloud and fog affecting atmospheric visibility, microbursts, and low-level jets leading to wind shear and clear air turbulence, are of crucial importance for flight safety and airport capacity [2,3].

Doppler lidars can make continuous and real-time 3D wind detection via Mie or Rayleigh backscatter [4]. In particular, coherent detection lidars (CDL) have been demonstrated successfully on ground-based [5,6], ship-based [7], and airborne [8] platforms. The CDL has matured over the past few decades, with very compact operational systems using eye-safe and solid-state lasers. In contrast to earlier coherent lidars based on free-space optics [9], the use of fiber-optic elements and integrated devices at working wavelengths of 1.5 or 2.0 μm offers practical advantages, including mechanical decoupling and remote installation of the subsystems, simplification of configuration and alignment, and enhancement in coupling efficiency and long-term stability [10,11].

An alternative method to the CDL for wind detection is direct detection Doppler lidar (DDL), which has been chosen by the European Space Agency as the unique instrument of the Atmospheric Dynamics Mission-Aelous [12]. The DDL shows several inherent advantages, such as an explicit sign of positive or negative Doppler shift, robust performance against wavefront distortion due to atmospheric turbulence and optics aberration, and the field of view of the telescope can be hundreds of times larger than the diffraction limited. A DDL is operated in a photon-counting mode, making it easy to record and process the raw data. The so-called double-edge technique permits the Rayleigh and Mie components of the backscatter to be independently determined [13], which is important for quantitative aerosol analyses [14]. The most challenging task in operating a

DDL is to realize a frequency locking of the Doppler shift discriminator to the working laser with a high precision (less than 1 MHz over the integrating time is usually required), making the DDL system complicated.

Now, it is well recognized that an all-fiber architecture is easy to adjust and mechanically reliable in harsh environments. The other advantages of an all-fiber architecture are their compactness and flexibility in terms of installation. Using an all-fiber architecture as in coherent lidars in communication band, a micropulse and versatile DDL is developed for wind and aerosol detection in the ABL. A double-edge technique is realized by using a single-channel all-fiber Fabry–Perot interferometer (FPI) and a single upconversion detector. The lidar can be divided into five subsystems (laser, circulator, telescope, scanner, and receiver), linked together using polarization maintaining fibers (PMFs), as illustrated in Fig. 1.

The laser adopts a master oscillator power amplifier structure. The continuous-wave laser from the distributed feedback diode (DFB, 1548.1nm) is chopped into the pulse train by using two lithium niobate intensity modulators (Photline, MXER-LN-10, bandwidth 10 GHz) in cascade, which suppresses the CW leakage to −70 dB and minimizes the amplified spontaneous emission (ASE) in the erbium-doped fiber amplifier. These two EOMs are driven and synchronized by using a pulse generator. The ASE is further suppressed by inserting a fiber Bragg grating with a bandwidth of 6 pm. Thus, the spectrum of the updated laser is purified, as shown in Fig. 2, where the pulse energy/duration is set to 50 μJ/200 ns. In contrast to a commercial available laser (Keyopsys, PEFA-EOLA), the updated laser shows a 20 dB lower ASE noise. The circulator is built up with a pair of Brewster plates and a piece of quarter-wave plate. Orthogonal staring observation at constant zenith is performed via a telescope (80 mm aperture) and a dual reflection scanner.

The atmospheric backscatter, combined with the reference pulse split out from the laser is fed to the optical receiver. An all-fiber, lensless, FPI (Micron Optics, C-band) is used as the frequency discriminator. The cavity is formed by two highly reflective multilayer mirrors that are deposited directly onto two carefully aligned optical fiber ends. An anti-reflection coated fiber inserted in the cavity provides appropriate confined light guiding. A stacked piezoelectric transducer (PZT) is used to axially strain the single-mode fiber inserted in the cavity. Thus, frequency scanning of the FPI can be achieved by changing the cavity length, as we introduced in the earlier DDLs [12,13].

The transmitted signal through the FPI is coupled into an upconversion detector (UPD), while the reflected signal is timely delayed, after propagating through a circulator (C_2) and an 8 km PMF. By using an optical switch (OS, Agiltron, NS-2 × 2), the transmitted and reflected signals can be directed into the detector alternatively, incorporating a time-division multiplexing (TDM) technique.

As shown in Fig. 1, inserts show pictures of the FPI and the UPD. The lidar adopts a polarization maintaining structure, except that the FPI is made of a single-mode fiber. However, this can be compensated for by adding two polarization controllers, one at the front and the other at the rear end of the FPI. The principle and manufacture of the UPD has been introduced elsewhere recently [15–17]. Here, the UPD is integrated into an all-fiber module, in which the periodically poled lithium niobate waveguide (PPLN-W) is coupled into a PMF/multi-mode fiber (MMF) at the front/rear end. An in-line interferometric filter with a bandwidth of 1 nm is inserted between the PPLN-W and the Si-APD. Using a pump laser at 1950 nm, the backscatter photons at 1548.1 nm are converted to 863 nm via sum frequency generation. Although the conversion efficiency can approach a value larger than 99% [16], due to the limited quantum efficiency of Si-APD at 863 nm and the coupling losses, the final system efficiency of the UPD is 20% with a dark noise of 300 counts per second. We emphasize that, due to the lowest attenuation (<0.3 dB/km) at 1.5 μm in fiber, an all-fiber FPI can be manufactured with very low insert loss (<0.3 dB). The all-solid structure of the FPI makes it immune to the ambient fluctuation of the atmospheric pressure. The TDM technique can only be implemented at the communication band. In other words, to the best of our knowledge, this is the most compact direct detection lidar.

In this Letter, a response function is defined as

$$Q(\nu) = [T(\nu) - R(\nu)]/[T(\nu) + R(\nu)], \quad (1)$$

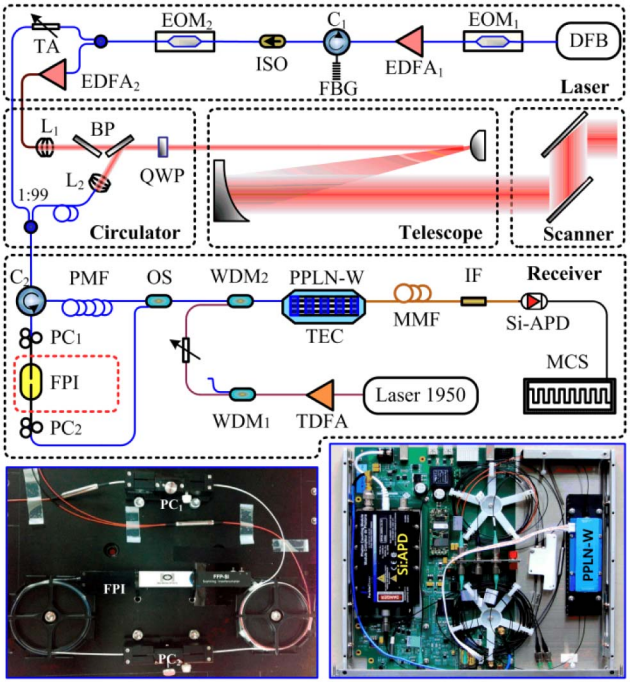

Fig. 1. Schematic of the compact Doppler lidar. TA, tunable attenuator; WDM, wavelength division multiplexer; L, lens; TDFA, thulium-doped fiber amplifier; TEC, thermos-electric cooler; MCS, multi-channel scaler.

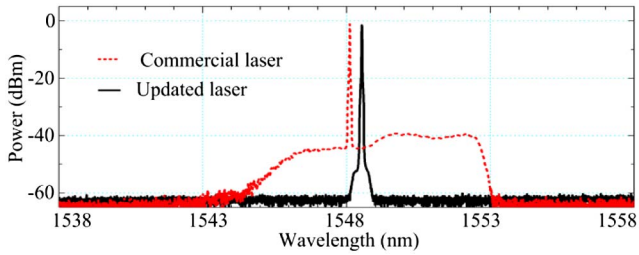

Fig. 2. Output spectra of the lasers. Note that the spectrum of the laser we built is right-shifted by 0.5 nm for an easy comparison.

where $T(\nu)$ and $R(\nu)$ are the transmission and reflection of backscatter on the FPI, respectively.

By scanning the voltage fed to the PZT in the FPI [18], the transmission and reflection curves are measured, as shown in Fig. 3(a). The response function is calculated. To test the stability of the integrated lidar, the response function is measured over nine weeks, as shown in Fig. 3(b). By applying Voigt fitting to the raw signal, the average full width at half-maximum is estimated to be 97.6 MHz with a relative error less than 0.1%. With its novel architecture, in addition to the full use of the backscatter, the simplicity and stability are obtained relative to the conventional direct detection lidar. One should also note that the response value changes from −1 to 1, indicating a doubled sensitivity relative to our Doppler lidar built 10 years ago [13].

As shown in Fig. 1, a small fraction of the energy of the output laser is split out as the reference signal, realizing a frequency locking of the laser to the FPI with a precision of 0.1 MHz over every second. The lidar can be operated in either the wind detection mode or the aerosol detection mode, depending on the locking frequency of the laser relative to the FPI, as shown in Fig. 3(a). In the wind mode, the frequency of the output laser is locked at the cross-point, where the sensitivity is maximized. A minor Doppler shift of the backscatter will cause a large difference in the response function. In the aerosol mode, the laser is locked at the full-reflection point. The reflected backscatter is used for quantitative aerosol analyses.

The pulse repetition frequency (PRF = 12 kHz) of the laser implies a maximum unambiguous detection range of 12.5 km. The laser beam is pointed at four orthogonal azimuths in sequence with a constant zenith angle of 30°. The dwell time at each azimuth is 10 s. Taking the time for the scanner movement and the data processing into account, each radial wind detection costs 12.5 s. The wind speed and direction are calculated based on the assumption of a horizontally homogeneous wind field, using four orthogonal radial wind profiles. Thus, the wind detection period is 50 s. To demonstrate the ability of aerosol detection, after each circle of wind detection, the scanner is pointed to the north horizontally with a dwell time of 6 s for atmospheric visibility detection.

The raw lidar signals and wind profiles are plotted in Fig. 4. The error bars are derived by assuming that the detection noise is dominated by the photon counting fluctuation, which follows a Poisson distribution [13]. The tolerated error of the wind speed is 2 m/s in this Letter. Different from the horizontal backscatter, the raw signals drop dramatically at the altitude of about 2.5 km in the wind mode, which is due to the sharp decrease of aerosol concentration at the top of the ABL.

Continuous observations of the atmospheric wind and visibility are carried out on the campus of the University of Science and Technology of China (31.843°N, 117.265°E). The experiment started at 12:00 on April 29 and ended at 12:00 on May 1, 2016. The experiment results are shown in Fig. 5. The data inversion algorithms for the wind and visibility detections are not expounded here. One can find detailed algorithms elsewhere [13,16]. The temperature and humidity near the ground are also monitored for reference. The features of the ABL, such as the wind profiles and the depth of the layer, evolve continuously in response to the diurnal cycle of the surface heating and cooling. Following sunrise on April 30, a convective layer developed and grew through the morning, reaching a height near 1.6 km by midafternoon. Within the convective ABL, convection transported the heat to the capping inversion base, making the depth of the ABL in accordance with the temperature near the ground. However, after the sunset, the wind grew stronger with a large gradient, and the depth of a stratified ABL was elevated to a maximum of about 2.5 km. The experiment was stopped just before a thunder shower occurred at 13:30. A low-level jet stream is observed with a maximum speed of 7.8 m/s at an altitude of about 0.9 km, at 10:30 on May 1, 2016.

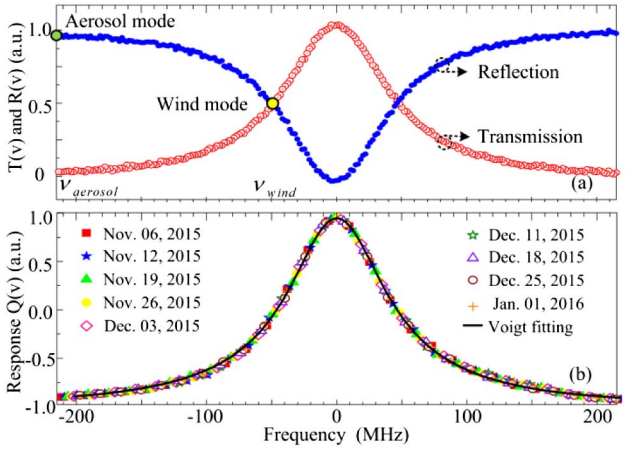

Fig. 3. (a) Transmission and reflection curves and (b) response functions measured over nine weeks and one typical Voigt fitting curve.

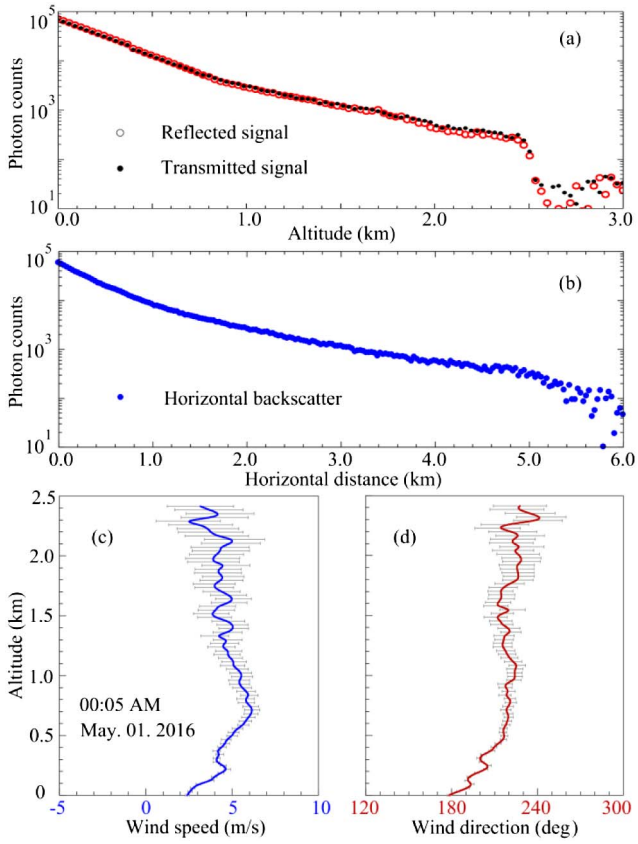

Fig. 4. Raw signals in (a) wind mode and (b) aerosol mode. (c) Wind speed (maximum error ±2 m/s) and (d) wind direction.

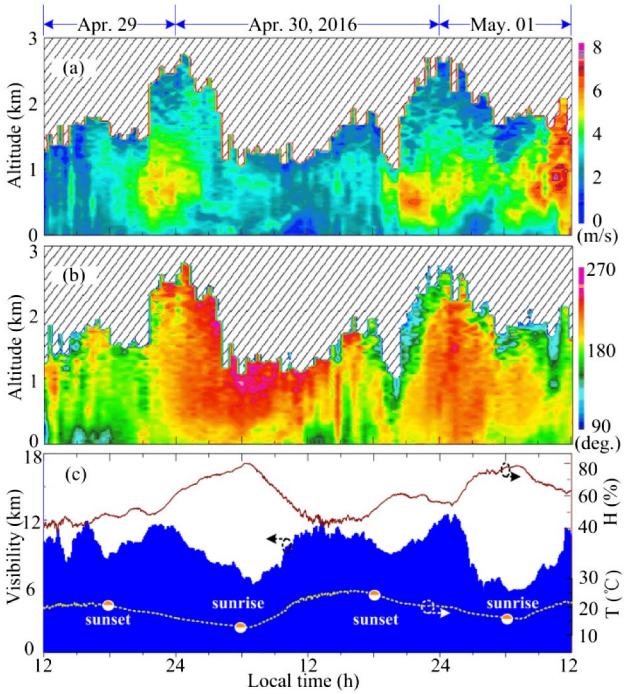

Fig. 5. Forty-eight-hour observation of atmospheric wind and visibility. (a) Wind speed, (b) direction, and (c) visibility, temperature, and humidity.

In the comparison experiment, an ultrasonic wind sensor (Vaisala windcap WMT52) is installed on a tower on the top of our building, with a height of 54 m above the ground. The temporal resolution is set to 1 min. The wind speed/direction

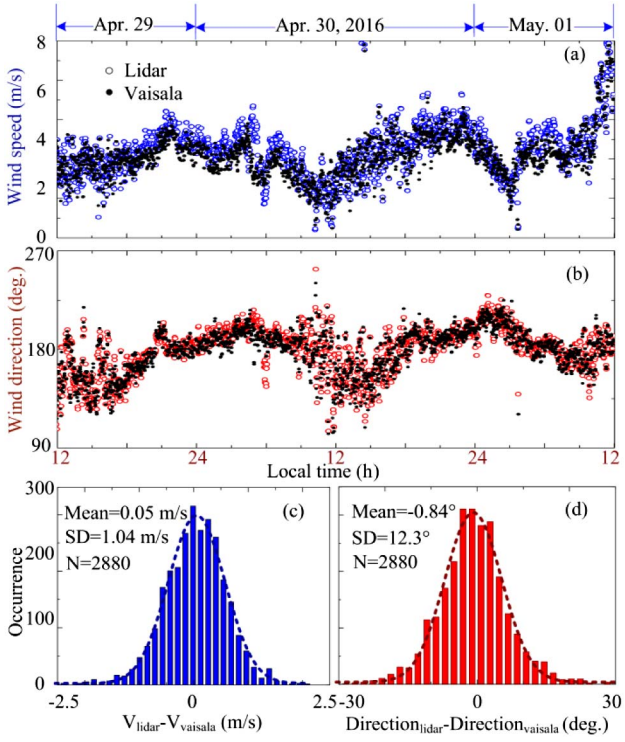

Fig. 6. Comparison experiment results. (a) Wind speed and (b) direction. Histograms of the differences of (c) speed and (d) direction.

accuracy is claimed to be ±3% at 10m/s and ±3°, respectively. In total, 2880 detection results are derived, as plotted in Fig. 6. Good agreements are observed. Histograms of the detection differences between the sensor and lidar are also plotted. The mean differences of the wind speed and direction are 0.05 m/s and −0.84°, and the standard deviations are 1.04 m/s and 12.3°.

In conclusion, a compact DDL is demonstrated, incorporating an upconversion, double-edge, and TDM techniques. Since the lidar adopts an all-fiber and polarization maintaining architecture, and uses a single-channel Fabry–Perot interferometer and only one upconversion single-photon detector, its system accuracy and stability are improved substantially.

Funding. National Natural Science Foundation of China (NSFC) (41274151, 41421063); Chinese Academy of Sciences (CAS) (KZZD-EW-01-1); National Fundamental Research Program (2011CB921300, 2013CB336800); 10000-Plan of Shandong Province; and the Fundamental Research Funds for the Central Universities.

Acknowledgment. The authors thank Dr. Mingyang Zheng and Dr. Xiuping Xie for their help in manufacturing the upconversion detector.

REFERENCES

1. J. R. Garratt, *The Atmospheric Boundary Layer*, Cambridge Atmospheric and Space Science Series (Cambridge University, 1992).
2. A. Dolfi-Bouteyre, B. Augere, M. Valla, D. Goular, D. Fleury, G. Canat, C. Planchat, T. Gaudo, C. Besson, A. Gilliot, J.-P. Cariou, O. Petilon, J. Lawson-Daku, S. Brousmiche, S. Lugan, L. Bricteux, and B. Macq, Aerosp. Lab. **1**, 1 (2009).
3. S. M. Hannon and J. A. Thomson, J. Mod. Opt. **41**, 2175 (1994).
4. C. Weitkamp, *LIDAR Range-Resolved Optical Remote Sensing of the Atmosphere* (Springer, 2006).
5. A. Dolfi-Bouteyre, G. Canat, M. Valla, B. Augere, C. Besson, D. Goular, L. Lombard, J. Cariou, A. Durecu, D. Fleury, L. Bricteux, S. Brousmiche, S. Lugan, and B. Macq, IEEE J. Sel. Top. Quantum Electron. **15**, 441 (2009).
6. G. J. Koch, J. Y. Beyon, B. W. Barnes, M. Petros, J. Yu, F. Amzajerdian, M. J. Kavaya, and U. N. Singh, Opt. Eng. **46**, 016002 (2007).
7. S. C. Tucker, W. A. Brewer, R. M. Banta, C. J. Senff, S. P. Sandberg, D. C. Law, A. M. Weickmann, and R. M. Hardesty, J. Atmos. Ocean. Technol. **26**, 673 (2009).
8. M. Kavaya, J. Beyon, G. Koch, M. Petros, P. Petzar, U. Singh, B. Trieu, and J. Yu, J. Atmos. Ocean. Technol. **31**, 826 (2014).
9. G. N. Pearson and C. G. Collier, Q. J. R. Meteorol. Soc. **125**, 2703 (1999).
10. N. S. Prasad, R. Sibell, S. Vetorino, R. Higgins, and A. Tracy, Proc. SPIE **9465**, 94650C (2015).
11. C. F. Abari, A. T. Pedersen, and J. Mann, Opt. Express **22**, 25880 (2014).
12. H. Xia, X. Dou, D. Sun, Z. Shu, X. Xue, Y. Han, and T. Cheng, Opt. Express **20**, 15286 (2012).
13. H. Xia, D. Sun, Y. Yang, F. Shen, J. Dong, and T. Kobayashi, Appl. Opt. **46**, 7120 (2007).
14. F. Chouza, O. Reitebuch, S. Groß, S. Rahm, V. Freudenthaler, C. Toledano, and B. Weinzierl, Atmos. Meas. Tech. **8**, 2909 (2015).
15. G. Shentu, J. S. Pelc, X. Wang, Q. Sun, M. Zheng, M. M. Fejer, Q. Zhang, and J. Pan, Opt. Express **21**, 13986 (2013).
16. H. Xia, G. Shentu, M. Shangguan, X. Xia, X. Jia, C. Wang, J. Zhang, J. S. Pelc, M. M. Fejer, Q. Zhang, X. Dou, and J. Pan, Opt. Lett. **40**, 1579 (2015).
17. L. Høgstedt, A. Fix, M. Wirth, C. Pedersen, and P. Tidemand-Lichtenberg, Opt. Express **24**, 5152 (2016).
18. M. Shangguan, H. Xia, C. Wang, J. Qiu, G. Shentu, Q. Zhang, X. Dou, and J. Pan, Opt. Express **24**, 19322 (2016).